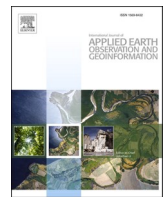




Contents lists available at ScienceDirect

International Journal of Applied Earth Observation and Geoinformation

journal homepage: www.elsevier.com/locate/jag



Early detection of pine shoot beetle attack using vertical profile of plant traits through UAV-based hyperspectral, thermal, and lidar data fusion

Qinan Lin ^{a,b,*}, Huaguo Huang ^b, Jingxu Wang ^c, Ling Chen ^b, Huaqiang Du ^a, Guomo Zhou ^a

^a State Key Laboratory of Subtropical Silviculture, Zhejiang A & F University, Hangzhou 311300, China

^b Research Center of Forest Management Engineering of State Forestry and Grassland Administration, Beijing Forestry University, Beijing 100083, China

^c Key Laboratory of Remote Sensing and Geographic Information System of Henan Province, Institute of Geography, Henan Academy of Sciences, Zhengzhou 450000, Henan, China



ARTICLE INFO

Keywords:

Pine shoot beetle
Early detection
Data fusion
Plant traits
Vegetation indices

ABSTRACT

Pine shoot beetle (PSB) is one of the most damaging forest insects of Yunnan pine plantations in southwest China. However, the subtle symptoms of heterogeneous tree crowns make it difficult to accurately detect at early stage of PSB attack. Here, we evaluated the potential of a combination of plant traits (PTs) and vegetation indices (VIs) to distinguish different levels of tree damage by integrating hyperspectral, thermal imagery, and light detection and ranging (lidar) data based on unmanned airborne vehicle (UAV) systems. A voxelization method was used to fuse hyperspectral reflectance, temperature, and lidar point cloud data. Subsequently, PTs such as pigments (i.e., chlorophyll, carotenoid, and anthocyanin contents) were retrieved from a radiative transfer model inversion, and structural, fluorescence, and thermal traits, as well as VIs, were derived from the fusion data. We developed a novel analytical approach using random forest (RF) algorithm with predictors from different spatial distributions (i.e., horizontal directions, vertical layers, and vertical clusters) to compare the performance of tree severity classification. The results showed that the difference of both PTs and VIs in vertical layers between different severity levels are more than that in horizontal directions. The performance of RF model with predictors of the vertical layers ($OA = 74\%$, $\kappa = 0.65$) was better than that using the predictive variables in horizontal directions ($OA = 69\%$ and $\kappa = 0.60$) of tree crowns. Using the vertical clustering features RF model increased the accuracy ($OA = 78\%$ and $\kappa = 0.70$), especially for slightly and moderately damaged trees, with improvements of 10% and 12%, respectively. Among all variables analyzed, chlorophylls were the most important predictor, followed by photochemical reflectance index and structural traits. Our work demonstrates the effectiveness of using fused UAV-based multi-sensor data for early detection of PSB attack, and can be applied to other potential forest diseases and insect monitoring.

1. Introduction

The pine shoot beetle (PSB) is acknowledged as one of the most dangerous and destructive forest insects of coniferous plantations in Southwest China (Lin et al., 2019; Yu et al., 2018). Yunnan pine is the most dominant host of PSB. PSB affects over five million hectares forests area, and leads to several million of trees were killed over the past forty years (Yu et al., 2022). Effective technology to monitor the progress of PSB outbreaks is essential to reduce forest destruction and economic losses.

To effectively monitor and mitigate the occurrence of PSB outbreaks, it is essential to have a comprehensive understanding of the life cycle of

PSB. Two stages of the PSB life cycle, shoot feeding and trunk grooving, have been reported by previous bioecological studies (Långström et al., 2002; Ye et al., 2004). During shoot-feeding stage, adult beetles initiate feeding within healthy shoots at treetops until they reach sexual maturity. As a consequence, tree crowns exhibit subtle symptoms, including limited shoot dieback and discoloration, which signify the early stage of PSB attack (Liu et al., 2021). During the trunk-grooving stage, beetles transfer to invade the tree trunk, which causes a high shoot dieback ratio (SDR) of the tree crown, ultimately resulting in the appearance of red and gray crowns (Yu et al., 2022). At this stage, the large population of PSB poses a significant challenge in preventing their outbreaks. Consequently, timely identification of PSB at the shoot-feeding stage is critical

* Corresponding author at: State Key Laboratory of Subtropical Silviculture, Zhejiang A & F University, Hangzhou 311300, China.

E-mail address: qinan.lin@zafu.edu.cn (Q. Lin).

to formulating effective pest management strategies.

Remote sensing is regarded as a non-contact technology that can help early diagnosis of vegetation stress by evaluating changes in plant traits (Foster et al., 2017; Hart and Veblen, 2015; Meddens et al., 2011; Senf et al., 2015; Ye et al., 2021). Plant traits (PTs), including leaf pigments (e.g., chlorophyll, carotenoid, and anthocyanin contents), water and dry matter contents, and crown structure, are closely associated with physiological processes and tree health (Hernández-Clemente et al., 2019). These PTs are promising indicators for the early detection of forest stress, as demonstrated by previous research (Chaturvedi et al., 2011; Hernández-Clemente et al., 2019; Hornero et al., 2020). RS methods offer an efficient solution for accurately retrieving PTs (Chapelle et al., 1992; Dronova et al., 2012; Ustin and Gamon, 2010; Woodward and Cramer, 1996). Especially, unmanned airborne vehicle (UAV) sensing systems, which integrate multiple sensors such as hyperspectral, thermal, and light detection and ranging (lidar), have the capability to generate exceptionally high spatial resolution images and high-density point clouds. These advanced features enable effective monitoring of insect-related forest disturbances at the individual tree level in a more precise manner (Fassnacht et al., 2014; Lin et al., 2019; Näsi et al., 2015). To quantify the important PTs, empirical strategies and the inversion of radiative transfer models (RTMs) are commonly used. Empirical strategies involved specific spectral bands or vegetation indices (VIs) to build linear models or machine learning (ML) models. RTM inversion commonly employed a look-up table (LUT) approach or a hybrid method that combined LUT with non-parametric regression models (e.g., ML). The application of empirical strategies is limited to specific spatial, temporal, and solar-viewing geometries. In contrast, RTMs are based on physical principles and are designed to model the intricate relationships among various factors, including canopy reflectance, crown structure, leaf optics, soil background, and solar-viewing geometry. These models provide a comprehensive framework for understanding and quantifying the complex interactions governing remote sensing observations.

Besides, VIs are widely used and developed with hyperspectral narrow bands to maximize sensitivity to vegetation stress. Zarco-Tejada et al. (2021) and Hornero et al. (2021) summarized nearly one hundred hyperspectral indices related to canopy structure (Chen, 1996; Haboudane et al., 2002; Roujean and Breon, 1995), pigment contents (Gitelson et al., 2006; Haboudane et al., 2002; Vogelmann et al., 1993), xanthophyll cycle (Gamon et al., 1992; Garrity et al., 2011; Hernández-Clemente et al., 2011), red/green/blue (R/G/B) band ratio (Lichtenthaler, 1996; Zarco-Tejada et al., 2012; Zarco-Tejada et al., 2018), nitrogen (Chen et al., 2010), chlorophyll fluorescence (Plascky and Gabriel, 1975), and vegetation temperature (Idso et al., 1981), serving as a proxy for tree health. Therefore, a semi-causal approach is to comprehensively integrate PTs with VIs for detecting forest diseases or insects (Hornero et al., 2021; Zarco-Tejada et al., 2018). This method offers greater robustness and generalizability to different environments for the accurate assessment of tree severity (Hornero et al., 2021).

To date, several investigations have assessed the fusion of hyperspectral and lidar data to derive biochemical, biophysical, and structural traits in monitoring tree decline (Dalagnol et al., 2019; Lin et al., 2019; Meng et al., 2018; Yu et al., 2021). However, most of these studies ignored the heterogeneity within damaged tree crown. Similar spectral characteristics between healthy canopies and low levels of damage severity (e.g., initial stage) will lead to incorrect estimates of the stage of tree infection if internal canopy heterogeneity is not considered (Hernández-Clemente et al., 2017). During the early stage of PSB attack, only a few damaged shoots are present at the top of the crown, while the majority of healthy shoots remain concentrated in the lower canopy (Lin et al., 2018; Lin et al., 2019; Liu et al., 2021; Yu et al., 2022). Although the effect of vertical heterogeneity on tree crown reflectance was partially addressed using a three-dimensional radiative transfer model RAPID (Huang et al., 2013) based on our previous studies (Lin et al., 2021), biochemical pigments from different vertical canopy layers

cannot be retrieved separately from UAV hyperspectral observations. Besides, other physiological indicators of plant health include sun-induced chlorophyll fluorescence (SIF) and crown temperature. These indicators are frequently employed as robust non-invasive tools for monitoring vegetation stress (Gonzalez-Dugo et al., 2019; Hornero et al., 2021; Zarco-Tejada et al., 2018). Moreover, Wang et al. (2022) highlighted that the temperature of vertical canopy layers was related to stomatal conductance and transpiration alterations, which are critical for early detection of PSB attack using thermal imagery. Shen et al. (2020) demonstrated that the combination of lidar and hyperspectral data was useful for quantifying the 3D distribution of biochemical pigments within tree crown. It provides new opportunities for the early detection of PSB attack at the tree level by integrating hyperspectral, thermal imagery, and lidar data.

In this study, we aim to quantify and assess the spatial distribution of PTs and VIs within tree crowns using fused hyperspectral, thermal, and lidar cloud point data to detect different levels of tree damage. By combining field measurements with UAV-based multi-sensor remote sensing data observations, we (1) explored the spatial distribution characteristics of PTs and VIs in different levels of tree damage; (2) developed an analytical approach to evaluate the performance of semi-causal method based on different spatial distributions of PTs and VIs as predictors; and (3) assessed the contribution of PTs and VIs for the early detection of PSB attack.

2. Material and methods

2.1. Field measurement

Our study site was located in Tianfeng Mountain ($25^{\circ}18'N$, $100^{\circ}27'E$) of Yunnan Province in China, covering an area of 1000 ha of Yunnan pine plantation. Three field plots were established between September 15–25, 2018, each with varying levels of tree crown damage. Four plots with varied sizes, including two 50×50 m plots, one 50×40 m plot, and one 200×50 m plot was measured (Fig. 1). A total of 1060 trees was measured. The coordinates of each tree position were measured utilizing an RTK system (HI-TARGET A8 GNSS) with high accuracy of 2.5 mm. To quantitatively assess pine tree damage, the shoot dieback ratio (SDR) and chlorophyll *a* and *b* content (C_{ab}) was employed. SDR (ranging from 0 to 100 %) is defined as the proportion of dead shoots to the total number of shoots for each damaged tree (Lin et al., 2021). The number of dead shoots for each tree was counted through visual inspection. Then, 3 ~ 6 branches were selected from different canopy heights to estimate the total number of shoots for entire tree. The severity of tree was categorized into four levels: healthy trees (SDR = 0), slightly damaged trees (SDR: 0 ~ 10 %), moderately damaged trees (SDR: 10 ~ 50 %), and severely damaged trees (SDR: >50 %) (Yu et al., 2018; Yu et al., 2022). To measure C_{ab} at crown level, four classes of the shoot-level C_{ab} was measured utilizing a calibrated chlorophyll content meter (CCM-300, Optisci, USA) based on the fluorescence ratio technique (Lin et al., 2018). The shoot-level C_{ab} was upscaled to the crown level by calculating the average C_{ab} across four shoots classes. Detailed information on calculation of crown level C_{ab} was described in Lin et al. (2021). The statistics of SDR and C_{ab} at crown level for four classes of Yunnan pine trees are shown in Table 1.

2.2. Uav-based remote sensing data collection and processing

UAV-based remote sensing data were obtained using a DJI Matrice 600 Pro hexacopter platform with an RTK system, incorporating hyperspectral, lidar, and thermal sensors during September 17–21, 2018 (Fig. 2). The lidar data were acquired using a LiAir-200 system (GreenValley International, California, USA) with integration of a Hesai Pandar40 scanner, an IMU and a differential GNSS system at a flight height of 70 m above ground. The lidar observation system was operated employing LiAcquire software (GreenValley International, California,

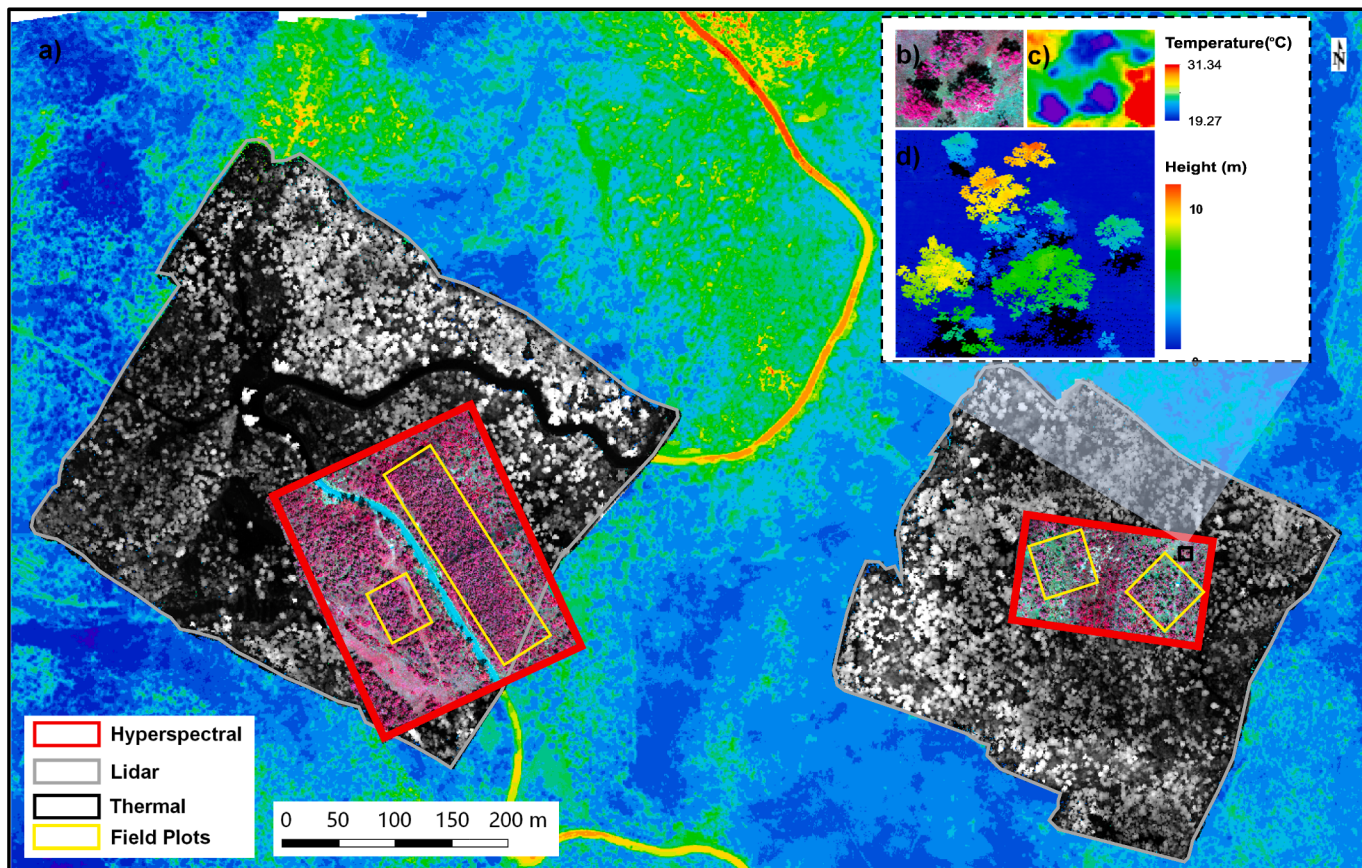


Fig. 1. Overview of UAV hyperspectral image (composite: 800 (R), 680 (G) and 540 (B) nm), DSM image, thermal image, and field plots location. Detailed views of Yunnan pine trees are showed in (b), (c), and (d) using hyperspectral, thermal and lidar sensors, respectively.

Table 1
Summary of SDR and C_{ab} of different severity level of tree crowns ($n = 1060$).

| Severity levels | n | SDR (%) | | | C_{ab} ($\mu\text{g}/\text{cm}^2$) | | |
|-----------------|-----|---------|-----------|--------|--|----------|-------------|
| | | Mean | Std. dev. | Range | Mean | Std. dev | Range |
| Healthy | 408 | 0 | 0 | 0 | 38.52 | 4.33 | 30.52–50.12 |
| Slight | 228 | 7.49 | 2.37 | 0–10 | 36.13 | 5.68 | 20.06–42.14 |
| Moderate | 220 | 38.18 | 5.63 | 10–50 | 23.48 | 6.05 | 13.65–32.72 |
| Severe | 204 | 85.67 | 6.58 | 50–100 | 11.16 | 4.02 | 0.50–21.22 |

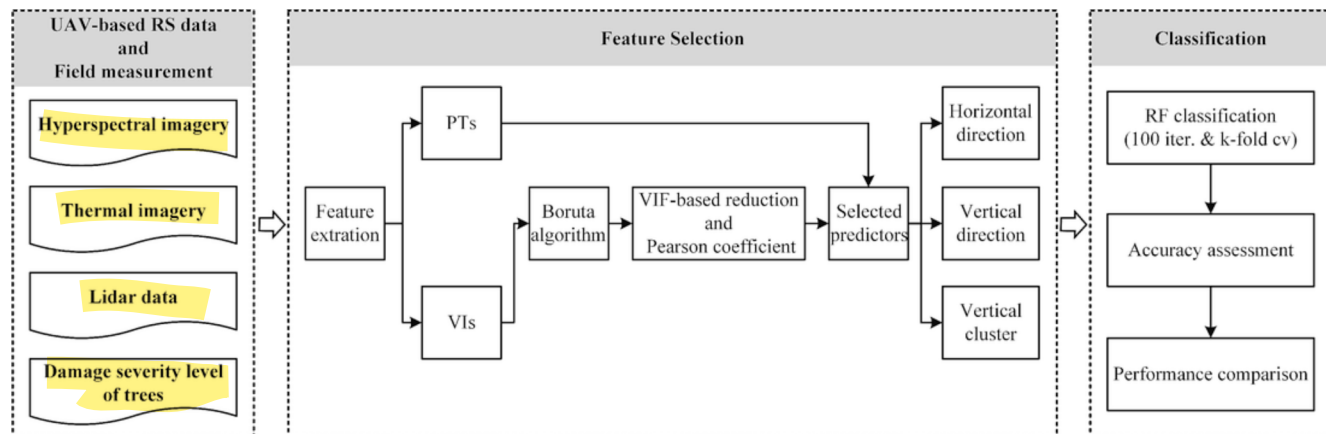


Fig. 2. The workflow of feature selection and tree classification.

USA), collecting point clouds with a density range from 200 to 1000 pulses m⁻². The lidar data were processed into standard products, including strip alignment, noise point removal, and ground point classification, using LiDAR 360 software (GreenValley International, California, USA). A digital elevation model (DEM) and digital surface model (DSM) were created with a spatial resolution of 0.20 m, using ground points and the highest canopy surface points, respectively. The DEM was used to normalize the elevation of the lidar point cloud. Subsequently, to segment individual tree for all plots, we used a point cloud segmentation algorithm developed by Li et al. (2012). The accuracy of tree segmentation (with an overall accuracy of 97 %) for three plots was systematically evaluated in our previous study (Lin et al., 2021). Finally, a total of 934 trees (tree height > 4 m) matched between field measurement and lidar segmentation were selected for further analysis, including 356 healthy trees, 206 slightly damaged trees, 204 moderately damaged trees, and 168 severely damaged trees.

The hyperspectral imagery was acquired utilizing the Nano Headwall VNIR Hyperspectral sensor with a push-broom observation system at flight attitude of 70 m. This sensor is equipped with a 17 mm focal length lens. It captures data across 270 spectral bands, covering a wavelength range of 400 to 1000 nm with a spectral sampling interval of 2.221 nm. During the flight campaign, the integration time was set to 10 ms and the flight speed was maintained at 3.5 m/s. The raw hyperspectral images were collected with a spatial resolution of 0.1–0.2 m. Radiance calibration of hyperspectral imagery were performed to convert raw data to radiance using Headwall's SpectralView software. The radiance bands were then converted to reflectance using the radiance spectrum of reference targets (Lin et al., 2021). Hyperspectral imagery was orthorectified with DEM data. After that, accurate geometric correction of mosaic imagery was conducted by ENVI 5.3 software with ten ground control points. Finally, the spatial resolution of hyperspectral mosaics was produced to 0.20 m.

The thermal imagery was acquired using the FLIR Tau 2 Longwave Infrared thermal sensor (FLIR Systems, Wilsonville, OR, USA) at a flight height of 280 m. The flight speed was set to 4 m/s and the time interval between acquisitions was 2 s, providing 60 % and 80 % overlap for side and forward, respectively. This sensor equipped with a 13 mm f/1.25 lens, which provides a field of view (FOV) of 45° × 35°, resulting in the acquired images with a spatial resolution range from 0.15 m to 0.23 m. After that, soil and known emissivity material target (i.e., polyvinyl chloride board, white wood, asphalt road) temperatures were measured using a handheld infrared thermometer (T-420, FLIR, USA) for vicarious calibrations (Wang et al., 2022). Finally, thermal imagery was mosaicked with spatial resolution of 0.2 m using Agisoft Metashape software to generate the entire forest scene of the study area.

2.3. Fusion of lidar point cloud, hyperspectral and thermal imagery

The voxelization of lidar data was used as a bridge to fuse lidar point cloud, hyperspectral and thermal imagery according to the method proposed by Shen et al. (2020). First, lidar-derived DSM, hyperspectral, and thermal imagery were co-registered to obtain the same spatial resolution (0.20 m) and highest spatial agreement with an accuracy of less than 0.5 pixels. Next, the normalized lidar point of the entire scene was transformed into a collection of 3D voxels with a spatial resolution of 0.2 × 0.2 × 0.2 m to match the hyperspectral and thermal pixels in the horizontal direction. Finally, the height value of the highest non-air voxel within each vertical column was associated with hyperspectral and thermal pixels to be used later for extracting the vertical profiles of PTs.

2.4. Plant traits and hyperspectral vegetation indices

2.4.1. Plant traits

Four types of PTs, including biochemical pigments (C_{ab} , C_{ar} , and C_{anth}), SIF (NIRvR), crown temperature (T_c), and crown structure (leaf

area density, LAD), were selected to assess their discriminatory capability between different levels of tree damage. The delineation of tree crowns from lidar segmentation was applied to hyperspectral and thermal imagery to further extract plant functional traits. Sunlit tree crown pixels were used to calculate the average of crown reflectance and radiance spectra, as well as crown temperature (T_c). The object-based segmentation method was used to exclude soil and shadow pixels within each segmented crown (Lin et al., 2019). Furthermore, the edge pixels in each tree crown were discarded to avoid mixed effects. The four types of PTs were retrieved from UAV RS data at the pixel (or voxel) scale using:

(1) biochemical pigments retrieval using radiative transfer model inversion

The coupled canopy radiative transfer model (RTM), PROSAIL-D, was used to retrieve biochemical pigments based on the reflectance of each pure vegetation pixel. Here, each sunlit pure vegetation pixel of tree crowns was assumed to be a homogeneous medium. The PROSAIL-D consists of PROSPECT-D model (Féret et al., 2017) and 4SAIL model (Verhoef et al., 2007). A look-up table (LUT) was generated using the PROSAIL-D simulations. The input parameters of the PROSAIL-D model were assigned a uniform distribution. The ranges of leaf and canopy input parameters were constrained by field measurements and relevant literatures (Li et al., 2020; Lin et al., 2018; Lin et al., 2021; Zarco-Tejada et al., 2019), aiming to reduce potential ill-posed inversion. The soil reflectance was determined by calculating the average of the forest floor reflectance based on hyperspectral imagery (Lin et al., 2021). For sun-view geometry, the observer zenith angle (θ_o) and relative azimuth angle (ϕ) were assumed to be zero, and the solar zenith angle (θ_s) was determined based on UAV-hyperspectral acquisition. The parameterization of the LUT is summarized in Table 2. Finally, a LUT with a size of 10,000 combinations was generated. After that, each simulated canopy reflectance ($R_{canopy}(\lambda)$) was resampled (Equation (1)) to the UAV-hyperspectral band set resolution according to the spectral response function (SRF) defined by full width at half maximum values (6 nm) of the hyperspectral sensor.

$$R_{image}(band_i) = \frac{\int_{\lambda_1}^{\lambda_2} R_{canopy}(\hat{I}_{\lambda}) SRF(\hat{I}_{\lambda}) d(\hat{I}_{\lambda})}{\int_{\lambda_1}^{\lambda_2} SRF(\hat{I}_{\lambda}) d(\hat{I}_{\lambda})} \quad (1)$$

where R_{image} (band_i) refers to the simulated band reflectance of hyperspectral image, and λ_1 and λ_2 is the lower and upper limit of each band interval, respectively.

We adopted a hybrid inversion based on RTM in combination with 1D convolutional neural network (CNN) regression to estimate C_{ab} using simulation canopy reflectance and UAV observation reflectance in the 400–800 spectral region. The AlexNet model was used in this study. The architecture of AlexNet was adjusted to 1D spectral signal processing by

Table 2
Input parameters and ranges of PROSAIL-D used for generating the LUT.

| Type of parameters | Parameters | Unit | Nominal values & range |
|------------------------|---------------------------------------|---------------------|------------------------|
| Leaf | Structure parameter (N) | – | 1.5–2.5 |
| | Leaf mass per area (C_m) | g cm ⁻² | 0.005–0.035 |
| | Leaf chlorophyll content (C_{ab}) | µg cm ⁻² | 0.5–50 |
| | Equivalent water thickness (C_w) | cm | 0.01 |
| | Carotenoid content (C_{ar}) | µg cm ⁻² | 0–15 |
| | Anthocyanin content (C_{anth}) | µg cm ⁻² | 0–7 |
| | Leaf area index (LAI) | – | 0.25–3.5 |
| Canopy | Average leaf angle (ALA) | degree | 30–70 |
| | Hot spot size (hspot) | – | 0.01 |
| | Solar zenith angle (θ_s) | degree | 25 |
| Solar-viewing geometry | Observer zenith angle (θ_o) | degree | 0 |
| | Relative azimuth angle (ϕ) | degree | 0 |

Shi et al. (2022), which was proven to have good performance in biochemical parameters estimation in RTM inversion. The parameters of all layers of the adjusted AlexNet are showed in supplementary Table S1. All LUT simulations were randomly divided into two datasets, i.e., a training dataset (accounting for 70 %) and a validation dataset (accounting for 30 %). A nonlinear activation function of the Rectifier Linear Unit (ReLU) in our case was applied for lower computational cost and rapid convergence. The stochastic gradient descent algorithm was used to train the modified AlexNet model, where the internal weights of neurons were updated with the Adam optimizer. During the back-propagation process, the mean absolute error (MAE) was used as the cost function.

$$\text{MAE} = \frac{\sum_{j=1}^n \sum_{i=1}^3 |y_i - \hat{y}_i|}{n} \quad (2)$$

where y_i is the measured biochemical pigments content of each sample, \hat{y}_i is the predicted biochemical pigments content of each sample, and n is the number of all samples.

To evaluate the performance of hybrid inversion (i.e., RTM-CNN), the mean crown C_{ab} by averaging all selected pixels within each tree crown was compared to the field-measured values with the coefficient of determination (R^2) and the root mean square error (RMSE). Due to the lack of C_{ar} and C_{anth} measurements, the three-band based VIs model (here: RECR and mARI) proposed by Gitelson et al. (2006), which has been confirmed to have a close linear relationship with C_{ar} and C_{anth} , was used to assess the retrieval performance.

(2) SIF and thermal indicators.

The near-infrared radiance of vegetation (NIRvR) was the product of NDVI and upwelling NIR radiance (Eq., 2) (Dechant et al., 2020). NIRvR was calculated from UAV-hyperspectral imagery by averaging over the range of 600–650 for the red band and over the near-infrared plateau of 800–850 nm for the NIR band (Dechant et al., 2020). Crown temperature (T_c) was extracted from the thermal imagery for each tree crown.

$$\text{NIRvR} = \text{NDVI} \cdot \text{NIR}_{rad} \quad (3)$$

(3) Leaf area density.

The segmentation of lidar data provided the vertical profile of point density for analyzing tree crown structure. The normalized lidar point was transformed into voxelization, and then post-deliverables of tree crown structural metrics were derived using the R environment with the “leafR” package (Almeida et al., 2019a). The horizontal grain size of the voxel was set to 0.20 m. In this study, each lidar pulse was assumed to be vertically incident because the laser scanning angle was less than 10°. Therefore, the energy transmission rate of the lidar pulse was estimated by counting the number of lidar pulses that enter (P_e) and pass through (P_t) for a vertical column. The LAD ($\text{m}^2 \text{ m}^{-3}$) for each voxel was calculated using the Beer-Lambert law-based MacArthur-Horn equation (MacArthur and Horn, 1969):

$$\text{LAD}_i = \ln\left(\frac{P_e}{P_t}\right) \frac{1}{k\Delta Z} \quad (4)$$

where ΔZ is the vertical resolution of the voxel grid, fixed at 0.20 m. k is a Beer-Lambert Law extinction coefficient. Here, k is set to a constant value of 1. Consequently, the derived value represents an effective LAD, and the air voxels ($P_e = 0$) and occluded voxels ($P_t = 0$) were coded as no-data (NA) voxels.

2.4.2. Hyperspectral vegetation indices

To increase the dimensionality of the features, 75 hyperspectral VIs (supplementary Table S2) within VNIR regions (Hornero et al., 2021; Zarco-Tejada et al., 2021) were computed for sunlit pixels of each tree crown. These VIs were mainly related to crown structure, pigments, the epoxidation state of the xanthophyll cycle, chlorophyll fluorescence emission, and nitrogen content.

2.5. Changes in plant traits and vegetation indices with increasing tree severity

Based on fused data, the vertical and horizontal dimensions of PTs and VIs for stressed Yunnan pine trees were used to analyze the physiological and structural changes in tree crowns in response to different PSB attack stages. All PTs and VIs were all calculated from different spatial distributions: (1) horizontal directions and (2) vertical layers. For the sake of simplicity, the spatial arrangement of the tree crowns was divided into four horizontal directions (i.e., east (E), south (S), west (W), and north (N)) and three vertical layers, i.e., upper (normalized tree height: 0.7–1.0), middle (normalized tree height: 0.4–0.7), and bottom (normalized tree height: 0.2–0.4) canopy layers. However, the spectral information of dead shoots was easily obscured by the signature of dominant healthy shoots within each canopy layers, especially for slightly damaged trees. Therefore, all features of each layer were classified into two clusters using K-means method based on Euclidean distance. The two clusters largely represent dead and non-dead shoots for each vertical canopy layer (named as vertical cluster), which can enhance the discriminatory capability of the classification models to detect low severity levels of tree.

We assessed the effects of PSB attack on PTs and VIs over horizontal directions, vertical layers and vertical clusters of tree crown using ANOVA. One-way ANOVA was used to investigate whether there were significant differences between the horizontal directions and vertical canopy layers. To estimate the differences ($P < 0.05$) between different levels of tree damage, we employed the least significant difference (LSD) post hoc test for multiple comparisons.

2.6. Feature selection and tree classification

We aim to improve the reliability of classification model using additional information provided by VIs for the initial model based on PTs. To reduce the number of VIs and multicollinearity problem, feature selection was performed with a standard procedure. First, Boruta algorithm (Kursa and Rudnicki, 2010) based on random forest (RF) classifier (Breiman, 2001; Liaw and Wiener, 2002) to estimate iteratively (set at 100 iterations) the importance of features by comparing their importance between the original features and shadow features (randomly reconstructed from original ones). Only features marked “Confirmed” (features are significantly higher than their shadows) were selected in this study. Second, a multicollinearity analysis using the variance inflation factor (VIF) and Pearson’s correlation coefficient to determine the noncorrelated plant traits. The threshold of VIF and correlation coefficient were defined to 10 and 0.85, respectively. The process of feature selection was conducted using the average value of VIs of whole tree crowns. Once the final features (showed in Appendix A) were determined, the selected features were extracted in different spatial distribution of each crown. The feature selection and the development of classification model are shown in Fig. 2.

RF classifier was used to classify different levels of tree damage, using field measurements and different spatial distributions (i.e., horizontal, vertical and vertical clusters) features as predictors, respectively. The hyperparameters (i.e., n_estimators, max_features, and min_samples_leaf) of RF algorithm were tuned using Bayesian optimization. The importance of each predictor was normalized by dividing it by the highest value to compare the differences in different spatial distributions of features for tree severity classification. Each RF model was run over the dataset in 100 iterations. To mitigate overfitting problems, we employed ten-fold cross validation. Furthermore, a balance approach was applied to ensure the same ratio of samples selected from each class for each iteration. The classification accuracies of RF models were assessed using producer’s accuracy (PA), omission error (OE), user’s accuracy (UA), commission error (CE), overall accuracy (OA) and the kappa coefficient.

3. Results

3.1. Biochemical pigments content retrieval performance

The biochemical pigments content retrieval performance using the RTM-CNN inversion is shown in Fig. 3. For the training and validation dataset, three pigments had a good estimation accuracy with an R^2 higher than 0.95 and RMSE less than $1.15 \mu\text{g}/\text{cm}^2$ (supplementary Table S3). Compared to the field measurements, the trained model still showed good accuracy in predicting C_{ab} with an R^2 of 0.81 and an RMSE of $5.52 \mu\text{g}/\text{cm}^2$. Besides, the predicted C_{ar} and RECRI ($R^2 = 0.90$) or C_{anth} and mARI ($R^2 = 0.75$) all had a significant linear relationship ($P < 0.01$).

3.2. Change in plant traits and vegetation indices in different spatial distribution for PSB attack

Based on feature selection processing, PTs and VIs were most sensitive to PSB attack including Structural traits (STs, e.g., LAD and RDVI), chlorophylls (e.g., C_{ab} and TCARI), carotenoids (C_{ar} and RECRI), photochemical reflectance indices (PRIs, e.g., PRI_{m3}), red/green/blue (R/G/B, e.g., LIC3), SIF (NIRvR), and thermal (T_c). Statistics and ANOVA confirmed statistically significant differences ($P < 0.05$) of PTs and VIs in horizontal directions of tree crown across different severity levels. However, LSD post hoc test (Fig. 4) showed that most of the features did not show significant differences between four horizontal directions for each severity. The C_{ab} , C_{ar} , NIRvR, LAD, RDVI, TCARI, and RECRI showed negative trend with increasing PSB attack stage. In particular, the C_{ab} , C_{ar} , NIRvR, and LAD did not show statistical difference ($P < 0.05$) between healthy and slight damaged trees, and RDVI, TCARI, and RECRI have not significant difference ($P < 0.05$) between slightly and moderately damaged trees. The C_{anth} , T_c , PRI_{m3}, mARI, and LIC3 showed a positive trend with increasing PSB attack level, but most of them show small differences between healthy, slightly, and moderately damaged trees.

Statistical analysis and ANOVA of PTs and VIs in three vertical layers between different levels of tree damage were showed in Fig. 5. Overall, compared with horizontal directions, all features in three layers can better capture the changes in trees with increasing severity levels. Both PTs and VIs in three layers show significant difference ($P < 0.05$) within each severity level (supplementary Fig. S1-S2). For most of PTs and VIs, the difference between bottom layer and middle and upper layers decreased with increasing severity levels. The LSD post hoc test confirmed that the level of significant of PTs and VIs in middle and upper layers between different levels of tree damage were higher than that of bottom layer. However, most of features (e.g., C_{ab} , NIRvR, T_c , and TCARI) in the bottom layer did not distinguish well between healthy and

slightly damaged trees. The difference in the average value of PTs and VIs between different severity levels increased with increasing canopy height. Similarly, PTs and VIs (Fig. 6) of two vertical clusters in three canopy layers showed marked difference between four severity levels. The trend of all features in each vertical cluster was similar as the level of tree crown damage increased. For most of PTs and VIs, the level of significant between different severity levels was improved, especially for T_c and LAD. In addition, the significant difference between the different levels of tree damage was greater in cluster 1 than in cluster 2.

For different levels of tree damage, the mean and standard deviation of PTs and VIs in different spatial distributions were presented in Appendix B. This statistical range covered more than 80 % of the measurement sample and effectively represented the thresholds of PTs and VIs for different damage severity level of trees. For the horizontal direction, all features (the average of E, S, W, and N directions) were well discriminated in severe trees from other tree classes. However, the threshold range of most PTs (e.g., C_{ar} and C_{anth}) and VIs (e.g., TCARI and mARI) has large overlap between slightly and moderately damaged trees. For vertical layers, most of the features in upper layers improve the differentiation between different levels of tree damage. But the differentiation of T_c , LAD, and mARI between all vertical layers and horizontal direction showed the same, especially for slightly and moderately damaged trees. Most of PTs and VIs of Cluster 1 have similar performance to the features of vertical layers in separating different levels of tree damage. However, the threshold range of all features for bottom and middle layers of cluster 2 have a significant overlap between healthy, slight, and moderate levels.

3.3. Comparison of tree damage classification accuracies using horizontal and vertical canopy PTs

As mentioned above, predictors in four horizontal directions of tree crown had no difference in response to PSB attack. Therefore, the average of predictors between four horizontal directions was used to build RF models. The OA and kappa coefficient of three RF models with different dimension of predictors are shown in Fig. 7. The RF model with horizontal predictors obtained lower accuracy (OA = $69 \pm 1\%$, kappa = 0.60 ± 0.01) lower than RF model using vertical predictors (OA = $74 \pm 1\%$, kappa = 0.65 ± 0.01). When PTs and VIs of two vertical clusters were included in RF model, the performance increased to an average OA = $78 \pm 1\%$ and kappa = 0.70 ± 0.01 . Compared to the RF model with horizontal predictors, the PA of slightly and moderately damaged trees was higher than that of healthy and severely damaged trees, with improvements of 10 % and 12 %, respectively (Fig. 8(a)). Although healthy and severely damaged trees showed a slight improvement among three RF models, they have a good accuracy with both PA and UA

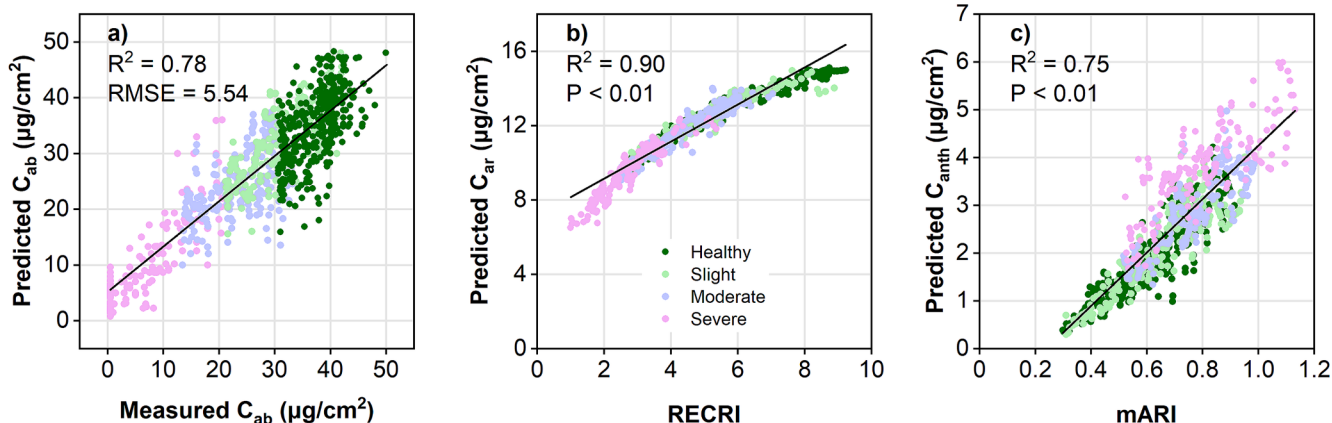


Fig. 3. Scatterplots between measured and predicted C_{ab} (a), RECRI and mARI calculated from hyperspectral images and predicted C_{ar} and C_{anth} derived from PROSAIL-D inversion (b-c).

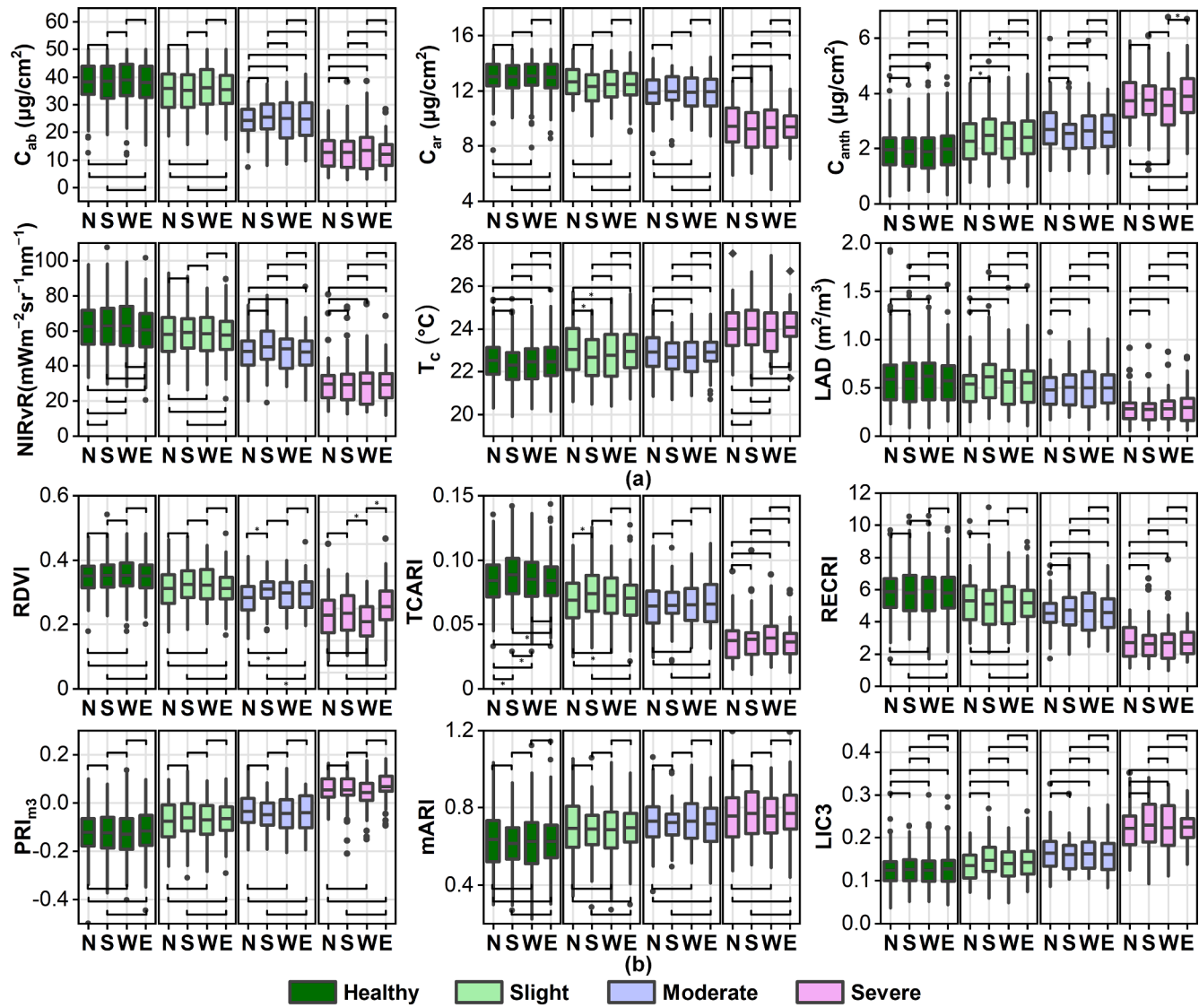


Fig. 4. Boxplots of the relationship between different levels of tree damage and plant traits (a) or vegetation indices (b) in four horizontal directions (i.e., east (E), south (S), west (W), and north (N)) which were derived from hyperspectral imagery. Level of significance: $*P < 0.05$ and $^{**}P < 0.01$.

approximately exceeding 80 % (Fig. 8). However, the highest classification errors (OE = 32 ~ 55 % and CE = 34 ~ 55 %) occurred in slightly damaged trees.

Variable importance for RF model based on PTs and VIs were presented in Fig. 9. For three RF models, Chlorophylls, PRIs, and STs had the highest contribution to models distinguishing tree severity under PSB attack. The contribution of all variables from middle and upper layers reached to 72 % when predictors in three vertical layers were included in RF model (Fig. 9b). Furthermore, cluster 1 features (account for 55 %) contributed more to the model than cluster 2 features (account for 45 %).

4. Discussion

4.1. Plant traits retrieval and uncertainty

We estimated three biochemical pigments (i.e., C_{ab} , C_{ar} , and C_{anth}), $NIRvR$, T_c and LAD from hyperspectral imagery, thermal imagery, and lidar data, and confirmed that these remotely-sensed PTs can contribute to PSB attack detection. Among them, C_{ab} , C_{ar} , and C_{anth} were retrieved from RTM-CNN inversion. Uncertainties in three biochemical pigments estimated by RTM-based hybrid inversion may propagate into predictive

RF models. Therefore, the realistic range of parameters from field measurements and related studies was used to constrain the LUT to alleviate the ill-posed problem. Despite the lack of comprehensive validation based on field measured data, good accuracy of C_{ab} estimation and high linear relationship between C_{ar} or C_{anth} and RECFI or mARI (Fig. 3) indicated the effectiveness of the hybrid inversion combined the AlexNet CNN model and PROSAIL-D simulation.

The $NIRvR$ and T_c were extracted from sunlit pure vegetation of tree crowns. The atmospheric reflectance correction and the effect of BRDF were ignored in UAV-based hyperspectral images processing due to clear sky conditions, low flight height (70 m) and narrow FOV (16°). This may introduce uncertainty in $NIRvR$ estimation for tree damage assessment. The extraction of T_c may be influenced by air temperature, as the narrow needles of the sparse canopy can introduce a mixing effect (Wang et al., 2022). To reduce this effect, the edge pixels of tree crown were discarded in this study. The accuracy of LAD estimation was affected by the trade-off between pulse density and grain size. Almeida et al., (2019b) found that higher pulse density resulted in higher LAD and LAI estimates in tropical forests, while this bias is small when pulse density exceeded 20 returns m^{-2} . Furthermore, the smaller grain size (<5 m) of the voxel showed better agreement with field measurements (Almeida et al., 2019b). Therefore, the smaller grain size was defined for Yunnan pines

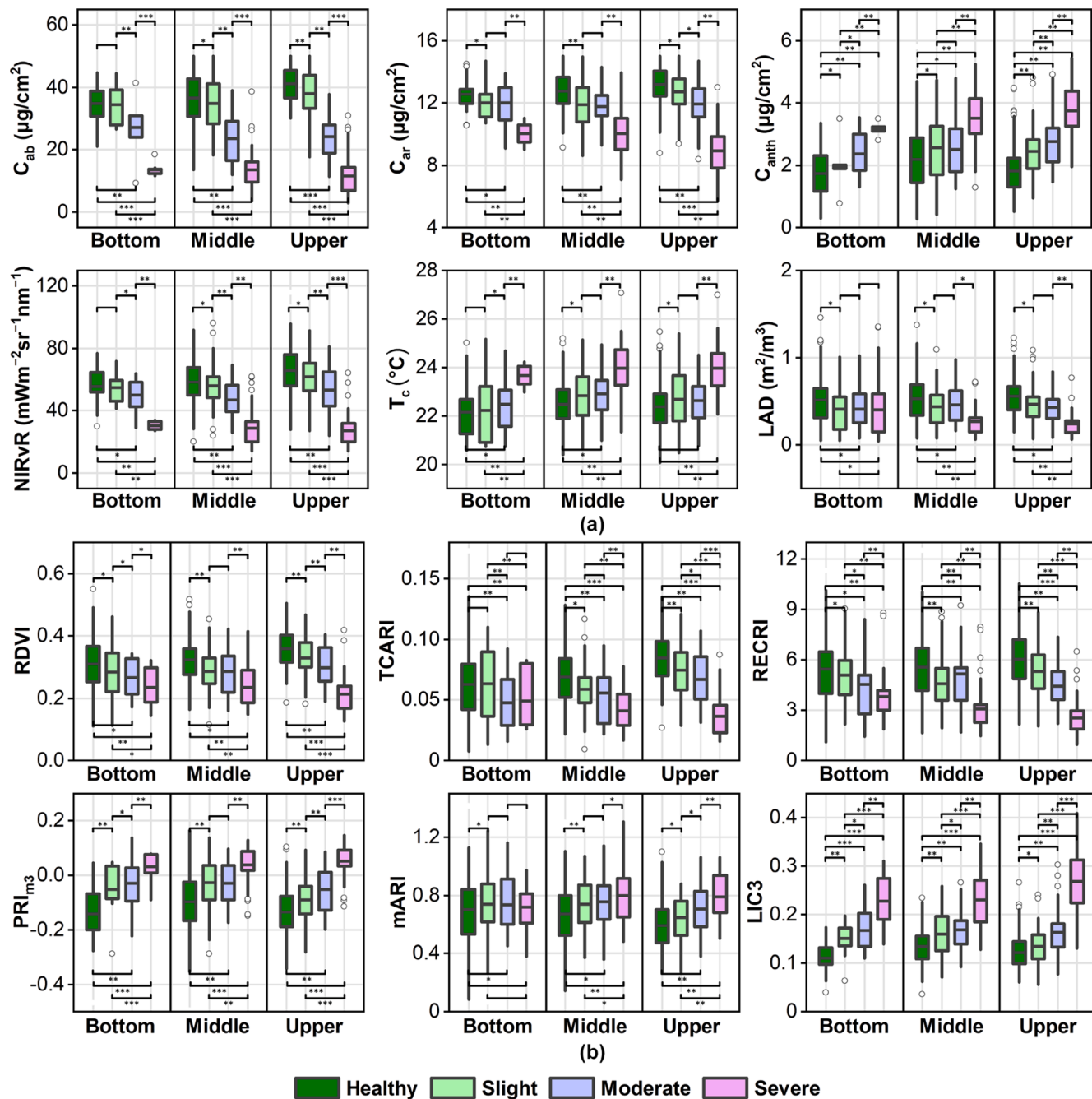


Fig. 5. Boxplots of plant traits (a) and vegetation indices (b) in three vertical layers (i.e., bottom, middle, and upper layers) for different levels of tree damage. Level of significance: * $P < 0.05$, ** $P < 0.01$, and *** $P < 0.001$.

to avoid violating of the MacArthur–Horn assumption of random leaf distribution due to the high leaf clumping within the tree crown of coniferous forest. Although multiple combinations of horizontal grain sizes and pulse density were not discussed in this study, the relative LAD values were useful for evaluating tree crown structure information when the shape of LAD profiles was applied (Almeida et al., 2019b).

4.2. Distribution of PTs and VIs at the tree crown to track changes in PSB attack

Our results indicated that the severity of PSB attack affected the PTs and VIs distribution within tree crown. For the horizontal directions of damaged tree crowns, the difference of PTs and VIs between healthy and slightly damaged trees were small. This was mainly due to the dominant

contribution of healthy shoots from the middle and bottom canopy layers to the whole tree crown, resulting in the similarity of spectral properties between damaged trees and healthy trees (Lin et al., 2019; Liu et al., 2021). In addition, the differences of all features in the four horizontal directions of tree crowns were not significant ($P < 0.05$). This result indicated that PSB attack within the crown had no directional tendency.

For vertical layers, the differences in all features between four severity levels were significant. In particular, most of features in the upper and middle canopy layers could track the differences between healthy trees and slightly damaged trees (Fig. 5). However, the difference of some features (e.g., T_c and LAD) between healthy, slightly, and moderately damaged trees were small. It was mainly caused by two reasons: (a) the number of damaged shoots is small and most of them

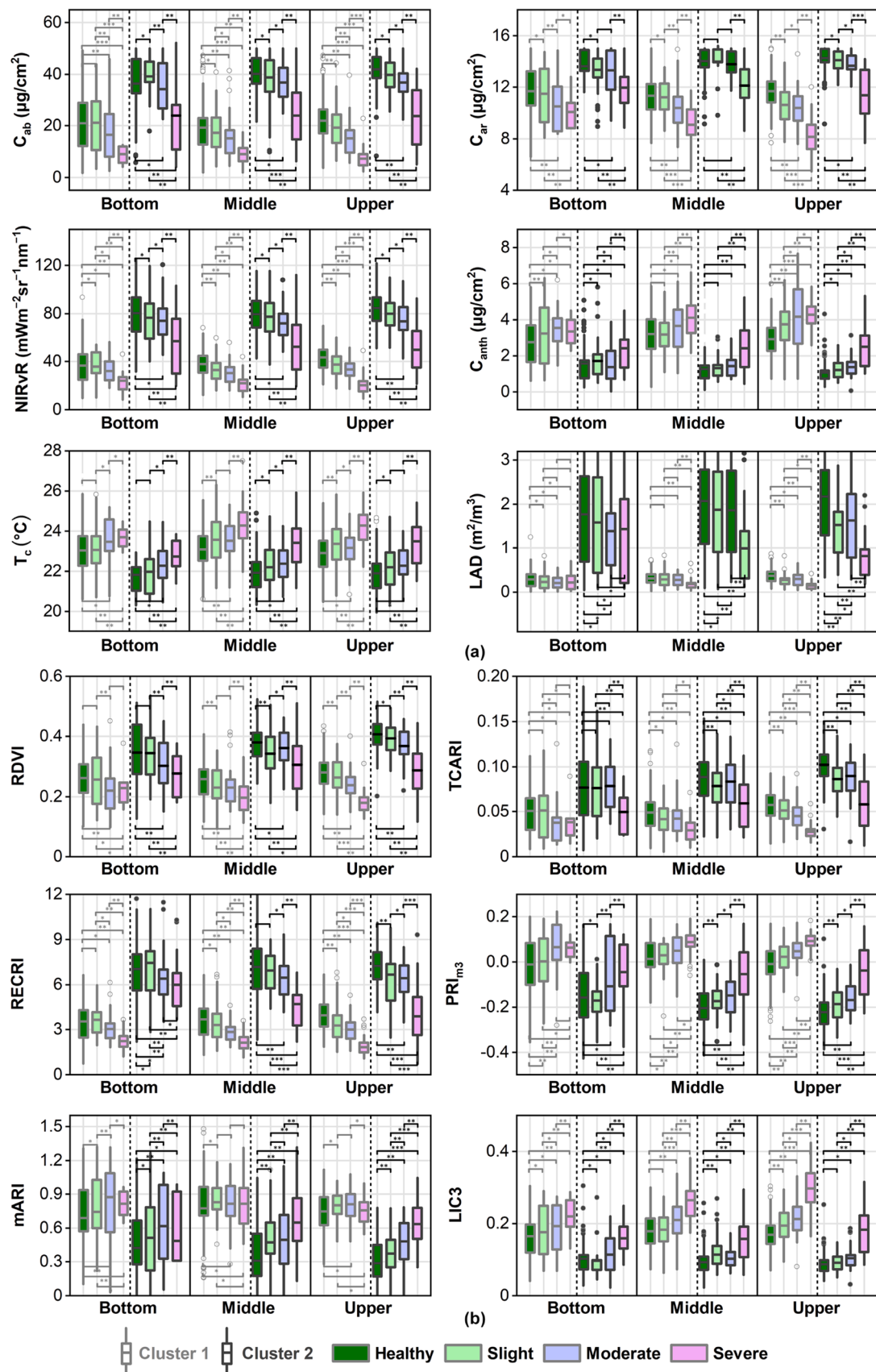


Fig. 6. Boxplots of plant traits (a) and vegetation indices (b) in different vertical clusters (i.e., bottom, middle, and upper canopy layers) for different levels of tree damage. Level of significance: * $P < 0.05$, ** $P < 0.01$, and *** $P < 0.001$.

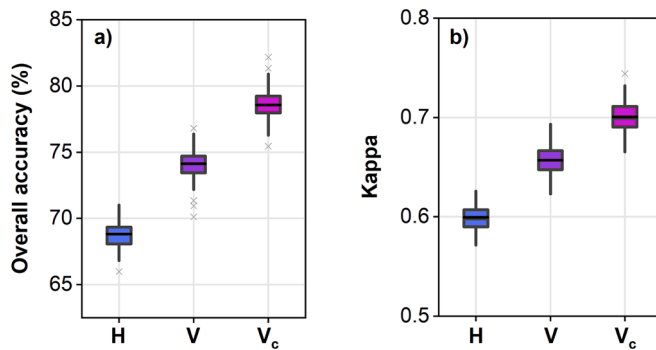


Fig. 7. Overall accuracy (a) and kappa (b) of RF models using different predictors: plant traits and vegetation indices in the horizontal (H) directions, vertical (V) layers, and vertical clusters (V_c) of tree crown.

distributed in the top of the canopy, and (b) crown structure changed slightly due the defoliation occurred in advanced severity levels. Vertical clustering method can effectively capture the subtle difference between low severity levels and healthy trees and improved their discrimination using PTs and VIs.

4.3. Pts and VIs contribution in RF models in tree severity mapping

The importance analysis of RF models revealed that all features contributed to discriminate different levels of tree damage by PSB attack. Chlorophylls obtained the largest contribution in the RF models. This results were consistent with previous related works on PSB detection (Lin et al., 2018; Lin et al., 2019; Liu et al., 2021), and other studies focusing on the VNIR (Camino et al., 2021; Hornero et al., 2020; Zarco-Tejada et al., 2018). These works remarked that pigments (e.g., chlorophylls, carotenoids, and anthocyanins) were more sensitive to leaf discoloration. PRIs, which were second most important predictors for distinguishing tree severity, were related to the epoxidation state of the xanthophyll cycle and photosynthetic efficiency (Hernández-Clemente et al., 2011; Sims and Gamon, 2002), and can be used to detect slight changes between healthy trees and slightly damaged trees.

SIF (i.e., NIRvR) and T_c were the last two importance variables to separate the damage severity level of trees in this study. Ample evidence has confirmed that canopy SIF retrieved from remote sensing data conveys leaf photosynthetic information and can be used to capture plant heat and water stress (Zarco-Tejada et al., 2018; Zeng et al., 2022). The T_c of middle and upper layers and vertical clusters 2 can help improve distinguishing the difference between healthy and slightly damaged trees. It caused by PSB stress disrupting the internal temperature regulation mechanism of the needles, such as the decrease in stomatal conductance and water potential (Gonzalez-Dugo et al., 2019;

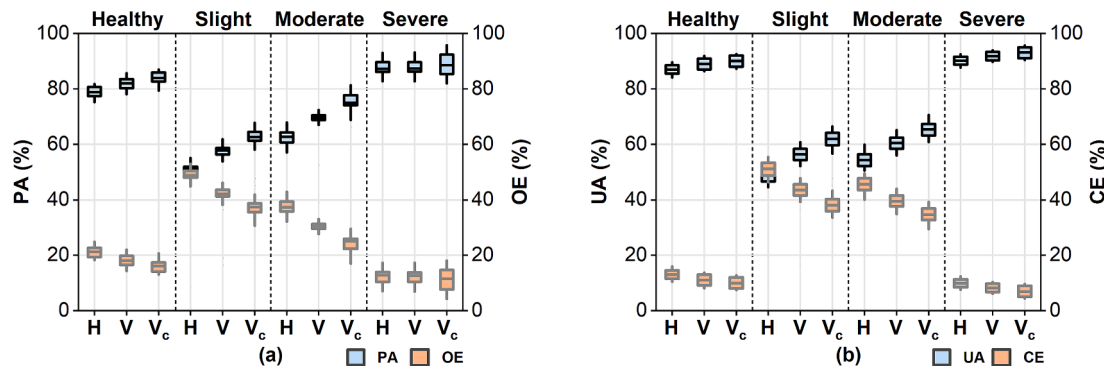


Fig. 8. Classification accuracy of each severity level of tree using RF models with different predictors.

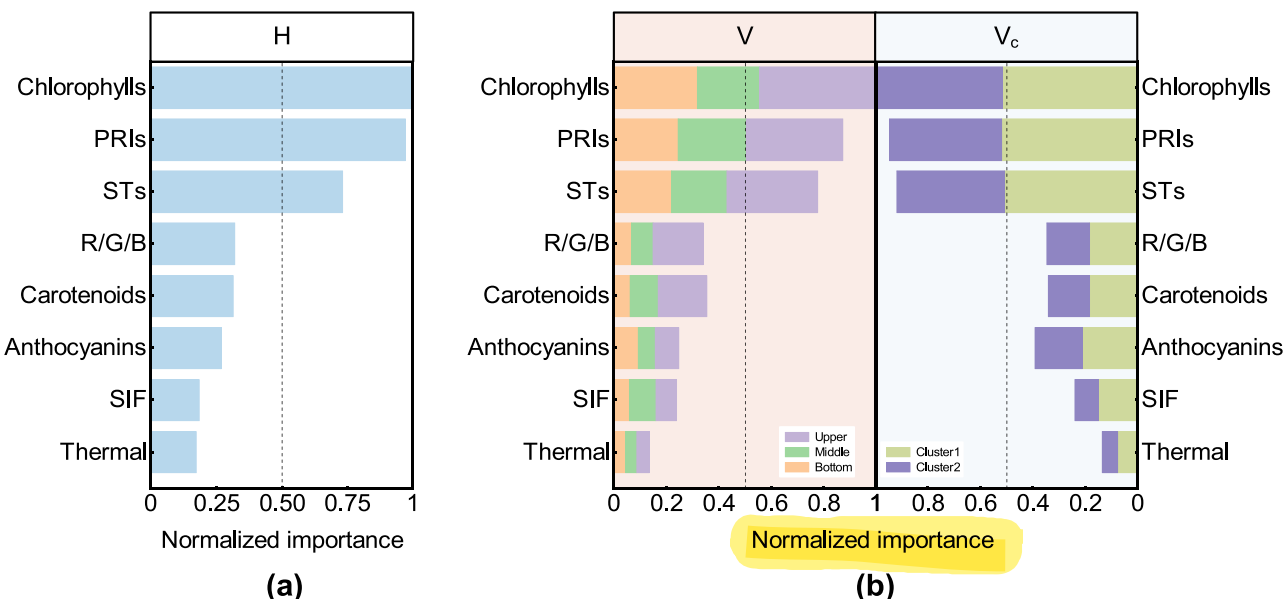


Fig. 9. Importance of plant traits and vegetation indices for RF models using: (a) horizontal (H) predictors, and (b) vertical (V) and vertical cluster (V_c) predictors.

Zarco-Tejada et al., 2013). However, the contribution of crown temperature may be weakened by the mixing effect of the surrounding air (Wang et al., 2022).

4.4. Potentiality of early detection of PSB through UAV-based multi-sensor data fusion

Early detection of PSB is essential to effectively mitigate the PSB attack on Yunnan pine forests. The hyperspectral and thermal imagery attained lower accuracy in early detection (with accuracy of $50 \pm 2\%$ for slightly damaged trees) because they lacked vertical structural information and therefore cannot detect the early symptoms in the upper canopy layer. Through combining the advantage between lidar and imagery sensors, vertical canopy features of damaged crowns were derived successfully, the classification accuracy of slightly damaged trees was improved (7—10%). This result confirmed that the vertical canopy features are better depicting the process change of heterogeneous crown than just considering the average value of whole tree crown for the detection of PSB attack. Although the contribution of crown temperature to tree severity modelling is lower than other features, the thermal imagery is another important source of [supplementary information](#) that enhances the potential for early detection. Overall, this study demonstrated that the early detection of PSB attack using multi-sensor data fusion is feasible. However, careful selection of features is critical and should be based on the sensitivity of specific spectral regions and plant traits to the symptoms of the PSB stress.

5. Conclusion

This study demonstrated that the combination of hyperspectral imagery, thermal imagery, and lidar point cloud data was useful for quantifying the spatial distribution of PTs and VIs to discriminate different levels of tree damage. Vertical layer features were more effective than horizontal direction features in distinguishing between healthy and mildly damaged canopy differences. The best results ($OA = 78\%$ and $\kappa = 0.70$) obtained for detection model using the

predictors of vertical clusters, with average accuracy of $84 \pm 2\%$ for healthy trees, $63 \pm 2\%$ for slightly damaged trees, $75 \pm 3\%$ for moderately damaged trees, and $89 \pm 3\%$ for severely damaged trees. Hyperspectral-derived chlorophylls was the most important indicators to discriminate between different damage severity levels, and followed by PRIs and STs. This study highlights the effectiveness of the vertical distribution of PTs and VIs retrieved from advanced UAV-based multi-sensor data fusion in the early detection of PSB attack, which can be extended to detect other harmful forest diseases and insects.

CRediT authorship contribution statement

Qinan Lin: Methodology, Software, Validation, Writing – original draft, Data curation. **Huaguo Huang:** Conceptualization, Investigation, Writing – review & editing. **Jingxu Wang:** Data curation, Formal analysis. **Ling Chen:** Writing – review & editing. **Huaqiang Du:** Resources, Supervision. **Guomo Zhou:** Resources, Supervision.

Declaration of Competing Interest

The authors declare that they have no known competing financial interests or personal relationships that could have appeared to influence the work reported in this paper.

Data availability

Data will be made available on request.

Acknowledgements

This work was supported by the National Natural Science Foundation of China (32301586), Natural Science Foundation of Zhejiang province (LQ22C160006), National Key R&D Program of China (2022YFD1400405), and Research Development Fund of Zhejiang A & F University (2020FR087). The authors would like to thank K. Huang and Y. Liu for the field measurement.

Appendix

Appendix A. . The final selected features including plant traits and vegetation indices were used in this study

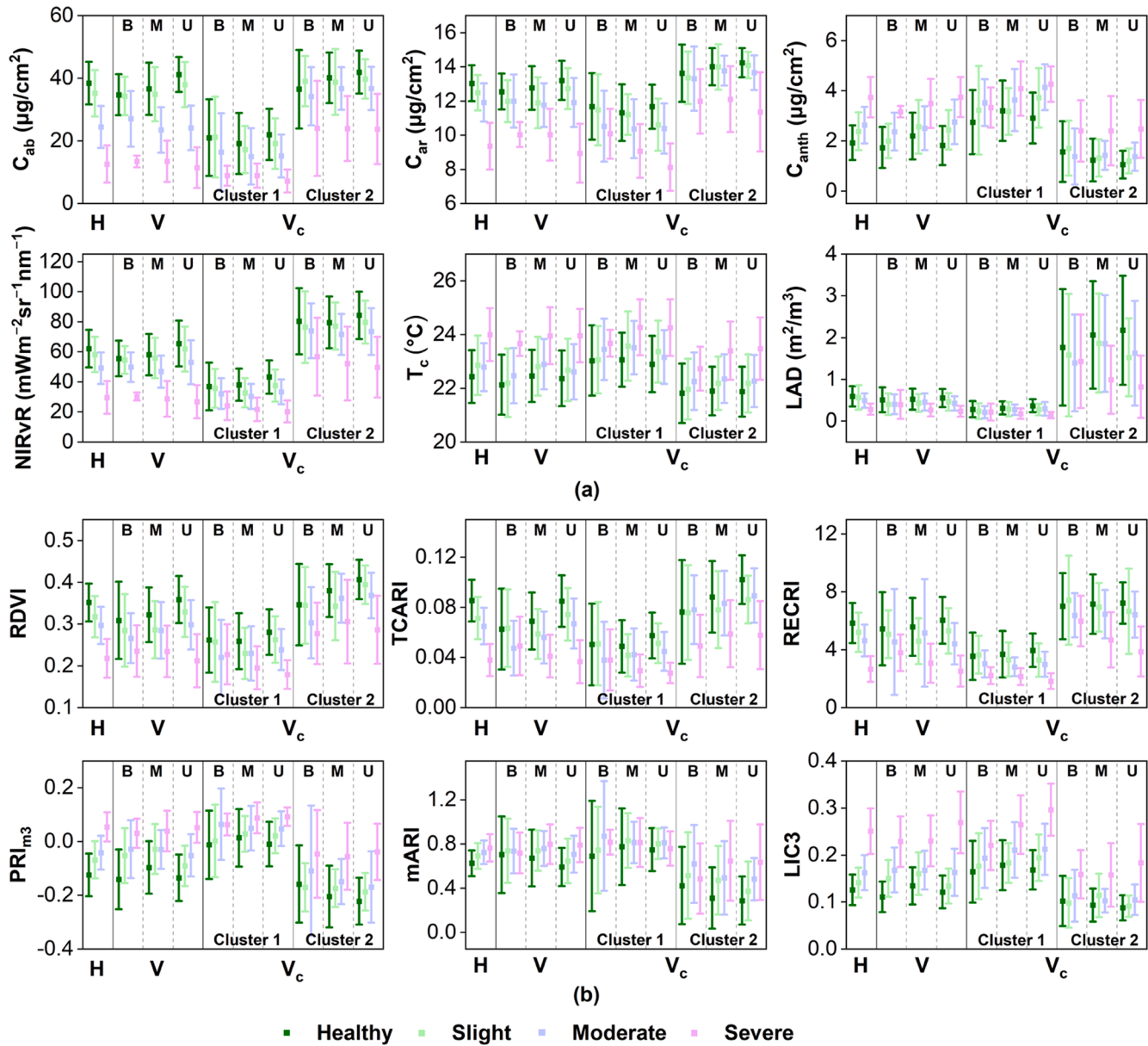
| Features | Equation/Source | Reference |
|---|---|---------------------------------|
| Structural traits (STs) | | |
| Renormalized Difference Vegetation Index | $RDVI = (R_{800} - R_{670}) / \sqrt{(R_{800} + R_{670})}$ | Roujean and Breon, 1995 |
| Sample Ratio | $SR = R_{800} / R_{670}$ | Jordan, 1969 |
| Modified Simple Ratio | $MSR = (R_{800} / R_{600} - 1) / [(R_{800} / R_{670})^{0.5} + 1]$ | Chen, 1996 |
| Modified Chlorophyll Absorption Ratio Index | $MCARI = [(R_{700} - R_{670}) - 0.2(R_{700} - R_{550})] / (R_{700} / R_{670})$ | Haboudane et al., 2004 |
| Leaf Area Density | LAD was derived from lidar data | – |
| Chlorophylls | | |
| Vogelmann 1 | $VOG_1 = R_{740} / R_{720}$ | Vogelmann, 1993 |
| Vogelmann 3 | $VOG_3 = (R_{734} - R_{747}) / (R_{715} + R_{720})$ | Vogelmann, 1993 |
| Transformed Chlorophyll Absorption Ratio Index | $TCARI = 3[(R_{700} - R_{670}) - 0.2(R_{700} - R_{550})(R_{700} / R_{670})]$ | Haboudane et al., 2002 |
| Normalized Phaeophytinization Index | $NPQI = (R_{415} - R_{435}) / (R_{415} + R_{435})$ | Peñuelas et al., 1995 |
| Leaf chlorophyll content | C_{ab} was retrieved from PROSAIL-D inversion | – |
| Carotenoids | | |
| Red-edge based Carotenoids Reflectance index | $RECRE = [(1/R_{510:520}) - (1/R_{690:710})]R_{760:800}$ | Gitelson et al., 2006 |
| Leaf carotenoid content | C_{ar} was retrieved from PROSAIL-D inversion | – |
| Anthocyanins | | |
| Modified Anthocyanin Reflectance Index | $mARI = [(1/R_{540:560}) - (1/R_{690:710})]R_{760:800}$ | Gitelson et al., 2006 |
| Leaf anthocyanin content | C_{anth} was retrieved from PROSAIL-D inversion | – |
| Photochemical Reflectance Indices (PRIs) | | |
| Photochemical Reflectance Index 515 | $PRI_{515} = (R_{515} - R_{531}) / (R_{515} + R_{531})$ | Hernández-Clemente et al., 2011 |
| Modified Photochemical Reflectance Index 1 | $PRI_{m1} = (R_{512} - R_{531}) / (R_{512} + R_{531})$ | Gamon et al., 1992 |
| Modified Photochemical Reflectance Index 2 | $PRI_{m2} = (R_{600} - R_{531}) / (R_{600} + R_{531})$ | Gamon et al., 1992 |
| Modified Photochemical Reflectance Index 3 | $PRI_{m3} = (R_{670} - R_{531}) / (R_{670} + R_{531})$ | Gamon et al., 1992 |
| PRI _x CI | $PRI_{x_CI} = (R_{570} - R_{531}) / (R_{570} + R_{531}) (R_{760} / R_{700} - 1)$ | Garrity et al., 2011 |
| R/G/B | | |

(continued on next page)

(continued)

| Features | Equation/Source | Reference |
|-----------------------|--|---------------------|
| Lichtenthaler Index 1 | $LIC1 = (R_{800}-R_{680})/(R_{800} + R_{680})$ | Lichtenthaler, 1996 |
| Lichtenthaler Index 3 | $LIC3 = R_{440}/R_{740}$ | Lichtenthaler, 1996 |
| SIF | | |
| NIRvR | NIRvR was derived from hyperspectral images | - |
| Thermal traits | | |
| Crown temperature | T_c was derived from thermal images | - |

Appendix B. The mean and standard deviation of plant traits (a) and vegetation indices (b) in different spatial distributions (i.e., horizontal (H), vertical (V) and vertical clusters (V_c)) for different damage severity level of trees. B, M, and U refer to the bottom, middle, and upper canopy layers, respectively.



Appendix C. Supplementary data

Supplementary data to this article can be found online at <https://doi.org/10.1016/j.jag.2023.103549>.

References:

- Almeida, D.R.A., Stark, S.C., Silva, C.A., Hamamura, C., Valbuena, R., 2019a. leafR: Calculates the Leaf Area Index (LAI) and other related functions. R Package 3. <http://CRAN.R-project.org/package=leafR>.
- Almeida, D.R.A.D., Stark, S.C., Shao, G., Schiatti, J., Nelson, B.W., Silva, C.A., Gorgens, E.B., Valbuena, R., Papa, D.D.A., Brancalion, P.H.S., 2019b. Optimizing the remote detection of tropical rainforest structure with airborne lidar: Leaf area profile sensitivity to pulse density and spatial sampling. *Remote Sens.* 11, 92. <https://doi.org/10.3390/rs11010092>.
- Breiman, L., 2001. Random forests. *Mach. Learn.* 45, 5–32. <https://doi.org/10.1023/A:1010933404324>.
- Camino, C., Calderón, R., Parnell, S., Dierkes, H., Chemin, Y., Román-Écija, M., Montes-Borrego, M., Landa, B.B., Navas-Cortes, J.A., Zarco-Tejada, P.J., Beck, P.S.A., 2021. Detection of *Xylella fastidiosa* in almond orchards by synergic use of an epidemic spread model and remotely sensed plant traits. *Remote Sens. Environ.* 260, 112420 <https://doi.org/10.1016/j.rse.2021.112420>.
- Chappelle, E.W., Kim, M.S., McMurtrey III, J.E., 1992. Ratio analysis of reflectance spectra (RARS): an algorithm for the remote estimation of the concentrations of chlorophyll a, chlorophyll b, and carotenoids in soybean leaves. *Remote Sens. Environ.* 39, 239–247. [https://doi.org/10.1016/0034-4257\(92\)90089-3](https://doi.org/10.1016/0034-4257(92)90089-3).
- Chaturvedi, R.K., Rahgabshahi, A.S., Singh, J.S., 2011. Plant functional traits with particular reference to tropical deciduous forests: A review. *J. Biosciences* 36, 963–981. <https://doi.org/10.1007/s12038-011-9159-1>.
- Chen, J.M., 1996. Evaluation of vegetation indices and a modified simple ratio for Boreal applications. *Can. J. Remote Sens.* 22, 229–242. <https://doi.org/10.1080/07038992.1996.10855178>.
- Chen, P., Haboudane, D., Tremblay, N., Wang, J., Vigneault, P., Li, B., 2010. New spectral indicator assessing the efficiency of crop nitrogen treatment in corn and wheat. *Remote Sens. Environ.* 114, 1987–1997. <https://doi.org/10.1016/j.rse.2010.04.000>.
- Dalagnol, R., Phillips, O.L., Gloor, E., Galvão, L.S., Wagner, F.H., Locks, C.J., Aragão, L.E., 2019. Quantifying canopy tree loss and gap recovery in tropical forests under low-intensity logging using VHR satellite imagery and airborne LiDAR. *Remote Sens.* 11, 817. <https://doi.org/10.3390/rs11070817>.
- Dechant, B., Ryu, Y., Badgley, G., Zeng, Y., Berry, J.A., Zhang, Y., Goulas, Y., Li, Z., Zhang, Q., Kang, M., 2020. Canopy structure explains the relationship between photosynthesis and sun-induced chlorophyll fluorescence in crops. *Remote Sens. Environ.* 241, 111733 <https://doi.org/10.1016/j.rse.2020.111733>.
- Dronova, I., Gong, P., Clinton, N.E., Wang, L., Fu, W., Qi, S., Liu, Y., 2012. Landscape analysis of wetland plant functional types: The effects of image segmentation scale, vegetation classes and classification methods. *Remote Sens. Environ.* 127, 357–369. <https://doi.org/10.1016/j.rse.2012.09.018>.
- Fassnacht, F.E., Latifi, H., Ghosh, A., Joshi, P.K., Koch, B., 2014. Assessing the potential of hyperspectral imagery to map bark beetle-induced tree mortality. *Remote Sens. Environ.* 140, 533–548. <https://doi.org/10.1016/j.rse.2013.09.014>.
- Féret, J.B., Gitelson, A.A., Noble, S.D., Jacquemoud, S., 2017. PROSPECT-D: Towards modeling leaf optical properties through a complete lifecycle. *Remote Sens. Environ.* 193, 204–215.
- Foster, A.C., Walter, J.A., Shugart, H.H., Sibold, J., Negron, J., 2017. Spectral evidence of early-stage spruce beetle infestation in Engelmann spruce. *Forest Ecol. Manag.* 384, 347–357. <https://doi.org/10.1016/j.foreco.2016.11.004>.
- Gamon, J.A., Penuelas, J., Field, C.B., 1992. A narrow-waveband spectral index that tracks diurnal changes in photosynthetic efficiency. *Remote Sens. Environ.* 41, 35–44. [https://doi.org/10.1016/0034-4257\(92\)90059-S](https://doi.org/10.1016/0034-4257(92)90059-S).
- Garrity, S.R., Etel, J.U.H., Vierling, L.A., 2011. Disentangling the relationships between plant pigments and the photochemical reflectance index reveals a new approach for remote estimation of carotenoid content. *Remote Sens. Environ.* 115, 628–635. <https://doi.org/10.1016/j.rse.2010.10.007>.
- Gitelson, A.A., Keydan, G.P., Merlyak, M.N., 2006. Three-band model for noninvasive estimation of chlorophyll, carotenoids, and anthocyanin contents in higher plant leaves. *Geophys. Res. Lett.* 33, L11402. <https://doi.org/10.1029/2006GL026457>.
- González-Dugo, V., Lopez-Lopez, M., Espadafor, M., Orgaz, F., Testi, L., Zarco-Tejada, P., Lorite, I.J., Fereres, E., 2019. Transpiration from canopy temperature: Implications for the assessment of crop yield in almond orchards. *Eur. J. Agron.* 105, 78–85. <https://doi.org/10.1016/j.eja.2019.01.010>.
- Haboudane, D., Miller, J.R., Pattey, E., Zarco-Tejada, P.J., Strachan, I.B., 2004. Hyperspectral vegetation indices and novel algorithms for predicting green LAI of crop canopies: Modeling and validation in the context of precision agriculture. *Remote Sens. Environ.* 90, 337–352. <https://doi.org/10.1016/j.rse.2003.12.013>.
- Hart, S.J., Veblen, T.T., 2015. Detection of spruce beetle-induced tree mortality using high-and-medium-resolution remotely sensed imagery. *Remote Sens. Environ.* 168, 134–145. <https://doi.org/10.1016/j.rse.2015.06.015>.
- Hernández-Clemente, R., Navarro-Cerrillo, R.M., Suárez, L., Morales, F., Zarco-Tejada, P.J., 2011. Assessing structural effects on PRI for stress detection in conifer forests. *Remote Sens. Environ.* 115, 2360–2375. <https://doi.org/10.1016/j.rse.2011.04.036>.
- Hernández-Clemente, R., North, P.R.J., Hornero, A., Zarco-Tejada, P.J., 2017. Assessing the effects of forest health on sun-induced chlorophyll fluorescence using the FluorFLIGHT 3-D radiative transfer model to account for forest structure. *Remote Sens. Environ.* 193, 165–179. <https://doi.org/10.1016/j.rse.2017.02.012>.
- Hernández-Clemente, R., Hornero, A., Mottus, M., Penuelas, J., González-Dugo, V., Jiménez, J.C., Suárez, L., Alonso, L., Zarco-Tejada, P.J., 2019. Early Diagnosis of Vegetation Health From High-Resolution Hyperspectral and Thermal Imagery: Lessons Learned From Empirical Relationships and Radiative Transfer Modelling. *Curr. for Rep.* 5, 169–183. <https://doi.org/10.1007/s40725-019-00096-1>.
- Hornero, A., Hernández-Clemente, R., North, P.R.J., Beck, P.S.A., Boscia, D., Navas-Cortes, J.A., Zarco-Tejada, P.J., 2020. Monitoring the incidence of *Xylella fastidiosa* infection in olive orchards using ground-based evaluations, airborne imaging spectroscopy and Sentinel-2 time series through 3-D radiative transfer modelling. *Remote Sens. Environ.* 236, 111480 <https://doi.org/10.1016/j.rse.2019.111480>.
- Huang, H., Qin, W., Liu, Q., 2013. RAPID: A Radiosity Applicable to Porous IndividDual Objects for directional reflectance over complex vegetated scenes. *Remote Sens. Environ.* 132, 221–237. <https://doi.org/10.1016/j.rse.2013.01.013>.
- Idso, S.B., Jackson, R.D., Pinter, P.J., Reginato, R.J., Hatfield, J.L., 1981. Normalizing the stress-degree-day parameter for environmental variability. *Agric. Meteorol.* 24, 45–55. [https://doi.org/10.1016/0002-1571\(81\)90032-7](https://doi.org/10.1016/0002-1571(81)90032-7).
- Jordan, C.F., 1969. Derivation of Leaf-Area Index from Quality of Light on the Forest Floor. *Ecology* 50, 663–666. <https://doi.org/10.2307/1936256>.
- Kursa, M.B., Rudnicki, W.R., 2010. Feature selection with the Boruta package. *J. Stat. Softw.* 36, 1–13. <https://doi.org/10.18637/jss.v036.i11>.
- Långström, B., Lisha, L., Hongpin, L., Peng, C., Haoran, L., Hellqvist, C., Lieutier, F., 2002. Shoot feeding ecology of *Tomocis piniperda* and *T. minor* (Col., Scolytidae) in southern China. *J. Appl. Entomol.* 126, 333–342. <https://doi.org/10.1046/j.1419-0418.2002.00651.x>.
- Li, W., Guo, Q., Jakubowski, M.K., Kelly, M., 2012. A new method for segmenting individual trees from the lidar point cloud. *Photogramm. Eng. Rem. s.* 78, 75–84. <https://doi.org/10.14358/PERS.78.1.75>.
- Li, X., Huang, H., Shabanov, N.V., Chen, L., Yan, K., Shi, J., 2020. Extending the stochastic radiative transfer theory to simulate BRF over forests with heterogeneous distribution of damaged foliage inside of tree crowns. *Remote Sens. Environ.* 250, 112040 <https://doi.org/10.1016/j.rse.2020.112040>.
- Liaw, A., Wiener, M., 2002. Classification and regression by randomForest. *R News.* 2, 18–22.
- Lichtenthaler, H. K., 1996. Vegetation stress: an introduction to the stress concept in plants. *J. Plant Physiol.* 148, 4–14. Doi: 10.1016/S0176-1617(96)80287-2.
- Lin, Q., Huang, H., Yu, L., Wang, J., 2018. Detection of Shoot Beetle Stress on Yunnan Pine Forest Using a Coupled LIBERTY2-INFORM Simulation. *Remote Sens.* 10, 1133. <https://doi.org/10.3390/rs10071133>.
- Lin, Q., Huang, H., Wang, J., Huang, K., Liu, Y., 2019. Detection of Pine Shoot Beetle (PSB) Stress on Pine Forests at Individual Tree Level using UAV-Based Hyperspectral Imagery and Lidar. *Remote Sens.* 11, 2540. <https://doi.org/10.3390/rs11212540>.
- Lin, Q., Huang, H., Chen, L., Wang, J., Huang, K., Liu, Y., 2021. Using the 3D model RAPID to invert the shoot dieback ratio of vertically heterogeneous Yunnan pine forests to detect beetle damage. *Remote Sens. Environ.* 260, 112475 <https://doi.org/10.1016/j.rse.2021.112475>.
- Liu, Y., Zhan, Z., Ren, L., Ze, S., Yu, L., Jiang, Q., Luo, Y., 2021. Hyperspectral evidence of early-stage pine shoot beetle attack in Yunnan pine. *Forest. Ecol. Manag.* 497, 119505 <https://doi.org/10.1016/j.foreco.2021.119505>.
- MacArthur, R.H., Horn, H.S., 1969. Foliation profile by vertical measurements. *Ecology* 50, 802–804. <https://doi.org/10.2307/1933693>.
- Meddens, A.J., Hücke, J.A., Vierling, L.A., 2011. Evaluating the potential of multispectral imagery to map multiple stages of tree mortality. *Remote Sens. Environ.* 115, 1632–1642. <https://doi.org/10.1016/j.rse.2011.02.018>.
- Näsi, R., Honkavaara, E., Lytykäinen-Saarenmaa, P., Blomqvist, M., Litkey, P., Hakala, T., Viljanen, N., Kantola, T., Tanhuapää, T., Holopainen, M., 2015. Using UAV-based photogrammetry and hyperspectral imaging for mapping bark beetle damage at tree-level. *Remote Sens.* 7, 15467–15493. <https://doi.org/10.3390/rs71115467>.
- Peñuelas, J., Baret, F., Filella, I., 1995. Semi-empirical indices to assess carotenoids/chlorophyll a ratio from leaf spectral reflectance. *Photosynthetica* 31 (2), 221–230.
- Plascyk, J.A., Gabriel, F.C., 1975. The Fraunhofer Line Discriminator MKII-An Airborne Instrument for Precise and Standardized Ecological Luminescence Measurement. *IEEE t. Instrum. Meas.* 24, 306–313. <https://doi.org/10.1109/TIM.1975.4314448>.
- Roujeau, J.L., Breon, F.M., 1995. Estimating PAR absorbed by vegetation from bidirectional reflectance measurements. *Remote Sens. Environ.* 51, 375–384. [https://doi.org/10.1016/0034-4257\(94\)00114-3](https://doi.org/10.1016/0034-4257(94)00114-3).
- Senf, C., Plügsmacher, D., Wulder, M.A., Hostert, P., 2015. Characterizing spectral-temporal patterns of defoliator and bark beetle disturbances using Landsat time series. *Remote Sens. Environ.* 170, 166–177. <https://doi.org/10.1016/j.rse.2015.09.019>.
- Shen, X., Cao, L., Coops, N.C., Fan, H., Wu, X., Liu, H., Wang, G., Cao, F., 2020. Quantifying vertical profiles of biochemical traits for forest plantation species using advanced remote sensing approaches. *Remote Sens. Environ.* 250, 112041 <https://doi.org/10.1016/j.rse.2020.112041>.
- Shi, S., Xu, L., Gong, W., Chen, B., Qu, F., Tang, X., Sun, J., Yang, J., 2022. A convolution neural network for forest leaf chlorophyll and carotenoid estimation using hyperspectral reflectance. *Int. J. Appl. Earth. Obs.* 108, 102719 <https://doi.org/10.1016/j.jag.2022.102719>.
- Sims, D.A., Gamon, J.A., 2002. Relationships between leaf pigment content and spectral reflectance across a wide range of species, leaf structures and developmental stages. *Remote Sens. Environ.* 81, 337–354. [https://doi.org/10.1016/S0034-4257\(02\)00010-X](https://doi.org/10.1016/S0034-4257(02)00010-X).
- Ustin, S.L., Gamon, J.A., 2010. Remote sensing of plant functional types. *New. Phytol.* 186, 795–816. <https://doi.org/10.1111/j.1469-8137.2010.03284.x>.
- Verhoef, W., Jia, L., Xiao, Q., Su, Z., 2007. Unified optical-thermal four-stream radiative transfer theory for homogeneous vegetation canopies. *IEEE Trans. Geosci. Remote Sens.* 45, 1808–1822. <https://doi.org/10.1109/TGRS.2007.895844>.
- Vogelmann, T.C., 1993. Plant Tissue Optics. *Annu. Rev. Plant. Physiol. Plant. Mol. Biol.* 44, 231–251. <https://doi.org/10.1146/annurev.pp.44.060193.001311>.

- Wang, J., Meng, S., Lin, Q., Liu, Y., Huang, H., 2022. Detection of Yunnan Pine Shoot Beetle Stress Using UAV-Based Thermal Imagery and LiDAR. *Appl. Sci.* 12, 4372. <https://doi.org/10.3390/app12094372>.
- Woodward, F.I., Cramer, W., 1996. Plant functional types and climatic change: introduction. *J. Veg. Sci.* 7, 306–308. <https://doi.org/10.1111/j.1654-1103.1996.tb00489.x>.
- Ye, H., Lv, J., Lieutier, F., 2004. On the bionomics of *Tomicus minor* (Hartig) (Col., On the bionomics of *Tomicus minor* (Hartig) (Col., Scolytidae) in Yunnan Province. *Acta Entomol. Sin.* 223–228. <https://doi.org/10.3321/j.issn:0454-6296.2004.02.015>.
- Ye, S., Rogan, J., Zhu, Z., Hawbaker, T.J., Hart, S.J., Andrus, R.A., Meddens, A.J., Hicke, J.A., Eastman, R.E., Kulakowski, D., 2021. Detecting subtle change from dense Landsat time series: Case studies of mountain pine beetle and spruce beetle disturbance. *Remote Sens. Environ.* 263, 112560 <https://doi.org/10.1016/j.rse.2021.112560>.
- Yu, L., Huang, J., Zong, S., Huang, H., Luo, Y., 2018. Detecting Shoot Beetle Damage on Yunnan Pine Using Landsat Time-Series Data. *Forests* 9, 39. <https://doi.org/10.3390/F9010039>.
- Yu, R., Luo, Y., Zhou, Q., Zhang, X., Wu, D., Ren, L., 2021. A machine learning algorithm to detect pine wilt disease using UAV-based hyperspectral imagery and LiDAR data at the tree level. *Int. J. Appl. Earth. Obs.* 101, 102363 <https://doi.org/10.1016/j.jag.2021.102363>.
- Yu, L., Zhan, Z., Ren, L., Liu, Y., Huang, H., Luo, Y., 2022. Effects of stand and landscape level variables on shoot damage ratios caused by shoot beetles in Southwest China. *Forest. Ecol. Manag.* 507, 120030 <https://doi.org/10.1016/j.foreco.2022.120030>.
- Zarco-Tejada, P.J., González-Dugo, V., Berni, J.A., 2012. Fluorescence, temperature and narrow-band indices acquired from a UAV platform for water stress detection using a micro-hyperspectral imager and a thermal camera. *Remote Sens. Environ.* 117, 322–337. <https://doi.org/10.1016/j.rse.2011.10.007>.
- Zarco-Tejada, P.J., González-Dugo, V., Williams, L.E., Suarez, L., Berni, J.A., Goldhamer, D., Fereres, E., 2013. A PRI-based water stress index combining structural and chlorophyll effects: Assessment using diurnal narrow-band airborne imagery and the CWSI thermal index. *Remote Sens. Environ.* 138, 38–50. <https://doi.org/10.1016/j.rse.2013.07.024>.
- Zarco-Tejada, P.J., Camino, C., Beck, P., Calderon, R., Hornero, A., Hernández-Clemente, R., Kattenborn, T., Montes-Borrego, M., Susca, L., Morelli, M., 2018. Previsual symptoms of *Xylella fastidiosa* infection revealed in spectral plant-trait alterations. *Nat. Plants.* 4, 432–439. <https://doi.org/10.1038/s41477-018-0189-7>.
- Zarco-Tejada, P. J., Poblete, T., Camino, C., Gonzalez-Dugo, V., Calderon, R., Hornero, A., Hernandez-Clemente, R., Román-Écija, M., Velasco-Amo, M. P., Landa, B. B., Beck, P. S. A., Saponari, M., Boscia, D., Navas-Cortes, J. A., 2021. Divergent abiotic spectral pathways unravel pathogen stress signals across species. *Nat. Commun.* 12 (1), 6088. Doi: 10.1038/s41467-021-26335-3.
- Zarco-Tejada, P.J., Hornero, A., Beck, P., Kattenborn, T., Kempeneers, P., Hernández-Clemente, R., 2019. Chlorophyll content estimation in an open-canopy conifer forest with Sentinel-2A and hyperspectral imagery in the context of forest decline. *Remote Sens. Environ.* 223, 320–335. <https://doi.org/10.1016/j.rse.2019.01.031>.
- Zeng, Y., Chen, M., Hao, D., Damm, A., Badgley, G., Rascher, U., Johnson, J.E., Dechant, B., Siegmann, B., Ryu, Y., Qiu, H., Krieger, V., Panigada, C., Celesti, M., Miglietta, F., Yang, X., Berry, J.A., 2022. Combining near-infrared radiance of vegetation and fluorescence spectroscopy to detect effects of abiotic changes and stresses. *Remote Sens. Environ.* 270, 112856 <https://doi.org/10.1016/j.rse.2021.112856>.